Supplementary Information (SI) for Chemical Communications.
This journal is © The Royal Society of Chemistry 2026

Electronic Supplementary Information

Electronic Structure Modulation of CoN/TiC-C Nanoarray by Vanadium Doping for Enhanced Alkaline Oxygen Evolution

Yi Sun,[a] Weiye Shi,[a] Zhongbao Wang,[a] Xueyu Du,[b] Yan Zhang,[a,c] Chunqing Huo,*[a] Shengjue Deng*[a,c] and Shiwei Lin*[a]

[a] Department of Materials Science and Engineering, Hainan University, Haikou 570228, P. R. China

[b] School of Chemistry and Chemical Engineering, Hainan University, Haikou 570228, P. R. China

[c] Anhui Provincial Key Laboratory of Advanced Catalysis and Energy Materials, School of Chemistry and Chemical Engineering, Anqing Normal University, Anqing 246001, PR China

E-mail: chunqinghuo@hainanu.edu.cn; 184305@hainanu.edu.cn; linsw@hainanu.edu.cn

1. Experimental section

1.1 Materials

Ti_6Al_4V foil was purchased from Xinji Metal Materials Co., Ltd. Acetone (C_3H_6O, AR) and ethanol (C_2H_5OH, AR) were procured from Xilong Chemical Co., Ltd. Cobalt(II) nitrate hexahydrate ($Co(NO_3)_2·6H_2O$, 99 %, AR), ammonium fluoride (NH_4F, 98%, AR), urea (CH_4N_2O, 99 %, AR) and potassium hydroxide (KOH, 95 %, AR) were provided by Shanghai Macklin Biochemical Technology Co., Ltd. Ammonium metavanadate (NH_4VO_3, AR) and Nafion solution（5 %）were acquired from Shanghai Aladdin Biochemical Technology Co., Ltd. Ammonia（NH_3, 99.9 %）was obtained from Hainan Sharp Gas Co., Ltd. A commercial 20 wt% Pt/C catalyst was supplied by Shanghai Hushen Electric Co., Ltd.

1.2 Synthesis of electrocatalysts

1.2.1 Preparation of TiC-C subtrate

Ti_6Al_4V foils (1 cm × 1.5 cm) were ultrasonicated in absolute ethanol for 15 min and rinsed with deionized water to remove surface contaminants. TiC-C nanostructures were then grown directly on the cleaned foils by chemical vapor deposition (CVD). The

foil was placed at the center of a horizontal tube furnace and heated to 850 °C at 10 °C min^{-1} under a 100 sccm argon flow. Once the target temperature was reached, acetone vapor was introduced into the furnace and maintained for 2 h to initiate and control the nucleation and growth of the TiC-C branched network.

1.2.2 Preparation of V-$Co(OH)_2$/TiC-C

A precursor solution was prepared by dissolving 0.3637 g $Co(NO_3)_2 \cdot 6H_2O$, 0.1187 g NH_4F, 0.375 g $CO(NH_2)_2$ and 0.030 g NH_4VO_3 in 25 mL deionized water. After 30 min of magnetic stirring, a homogeneous, pale orange-yellow solution was obtained. A piece of pre-cleaned TiC-C substrate was immersed in this solution inside a Teflon-lined stainless-steel autoclave. The autoclave was heated to 120 °C and held at this temperature for 6 h. Upon cooling to room temperature, the substrate was removed, rinsed sequentially with deionized water and ethanol, and dried at 70 °C for 12 h to remove residual solvent. To optimize the hydrothermal conditions, parallel runs were conducted with holding times of 4 h, 6 h and 8 h. $Co(OH)_2$/TiC-C was prepared under identical conditions without the addition of NH_4VO_3.

1.2.3 Preparation of V-CoN/TiC-C

V-CoN/TiC-C was obtained by ammonia annealing of the V-$Co(OH)_2$/TiC-C precursor. The precursor was loaded into the central zone of a quartz tube furnace and heated under flowing NH_3 (200 sccm, 400 °C, 2 h, ramp 5 °C min^{-1}), followed by natural cooling to ambient temperature. An identical procedure, omitting NH_4VO_3 during hydrothermal synthesis, yielded undoped CoN/TiC-C nanoarrays. To identify optimal conditions, additional runs were conducted at 400 °C and 450 °C with dwell times of 90, 120, 150 and 180 min.

1.2.4 Preparation of IrO_2/TiC-C

IrO_2/TiC-C was prepared by drop-casting. A homogeneous ink was first obtained by dispersing 2 mg IrO_2 in 380 μL isopropanol containing 20 μL Nafion solution (5 wt %) under sonication for 30 min. Subsequently, 100 μL of the ink was applied onto a 1 cm^2 TiC-C substrate and allowed to dry in air at ambient temperature.

1.3 Characterization of electrocatalysts

The crystalline phases of the electrocatalysts were identified using grazing-

incidence X-ray diffraction (GIXRD) on a Panalytical Empyrean diffractometer, with measurements conducted over the 2θ range of 10–80°. Surface morphologies were examined using a JEOL JSM-7800F field-emission scanning electron microscope (SEM) and a JEOL JEM-2800 transmission electron microscope (TEM). Raman spectroscopy (10–3500 cm^{-1}) was performed on a Renishaw Invia Raman microscope using a 514 nm excitation laser. Chemical states were probed by X-ray photoelectron spectroscopy (XPS) on a Thermo Scientific ESCALAB 250Xi spectrometer with monochromatic Al Kα radiation.

1.4 Electrochemical measurements

All electrochemical evaluations were performed at room temperature in 1.0 M KOH using a CHI-660E potentiostat and a standard three-electrode cell. The as-prepared catalyst served as the working electrode, a Pt foil as the counter electrode, and Hg/HgO (1.0 M KOH) as the reference electrode. All potentials were converted to the reversible hydrogen electrode (RHE) scale using the Nernst equation: $E_{RHE}=E_{Hg/HgO}+0.098+0.059\times pH$.

Prior to linear sweep voltammetry (LSV), each electrode was activated by 10 cyclic voltammetry (CV) cycles between 0.924 and 1.924 V vs RHE at 100 mV s^{-1}. LSV data were then collected from 0.924 to 1.924 V vs RHE at 5 mV s^{-1} with 95 % iR compensation based on the ohmic resistance determined by electrochemical impedance spectroscopy (EIS). Tafel slopes were calculated from the iR-corrected polarization curves.

The electrochemically active surface area (ECSA) was derived from the double-layer capacitance (C_{dl}). CV were recorded in the non-faradaic region (0.824–0.924 V vs RHE) at scan rates of 20, 40, 60, 80 and 100 mV s^{-1}. The current density difference between the anode and the cathode ($\Delta j = j_{anodic} - j_{cathodic}$) at 0.874 V vs RHE was plotted against the scan rate, and the slope equals $2\times C_{dl}$. ECSA was then calculated as $ECSA=C_{dl}/C_s\times ASA$, where C_s = 0.040 mF cm^{-2} is the specific capacitance of the oxide surface and ASA is the geometric surface area (1 cm^2).

The electrochemical impedance test (EIS) measurements were conducted over 0.1 Hz–100 kHz with a 10 mV amplitude and a test area of 1 cm^2 at open-circuit potential.

Stability tests were carried out in a 1 cm² configuration. Cyclic durability was assessed by comparing LSVs recorded at 5 mV s^{-1} before and after 2,000 CV cycles between 1.5 and 1.8 V vs RHE (scan rate 100 mV s^{-1}). Long-term stability was evaluated by chronopotentiometry at 100 mA cm^{-2} for 65 h.

2. Supporting information

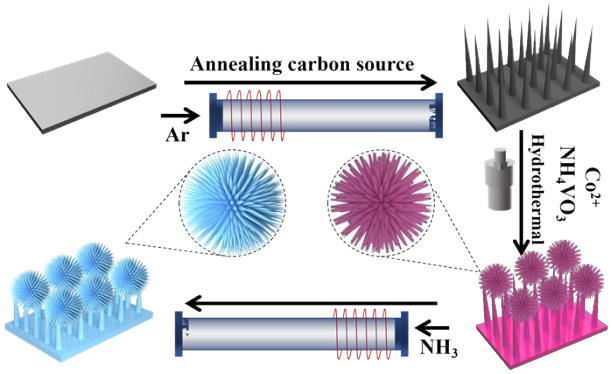

Scheme 1. Schematic of the synthesis of V-CoN/TiC-C

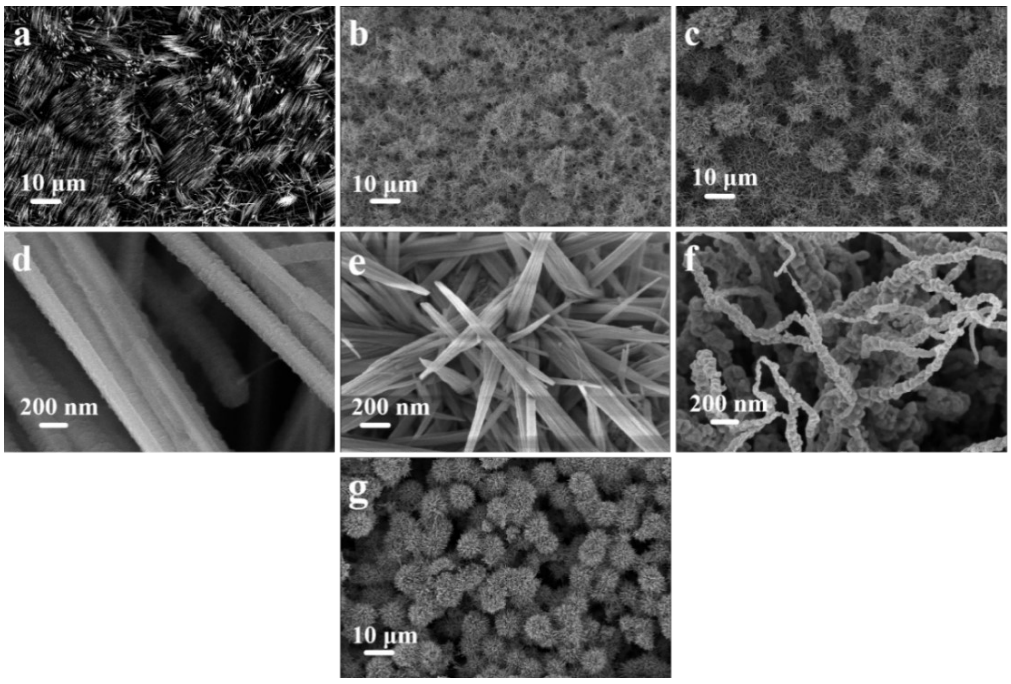

Fig. S1. SEM images of (a,d) TiC-C, (b,e) V-$Co(OH)_2$/TiC-C, (c,f) CoN/TiC-C and (g) V-CoN/TiC-C

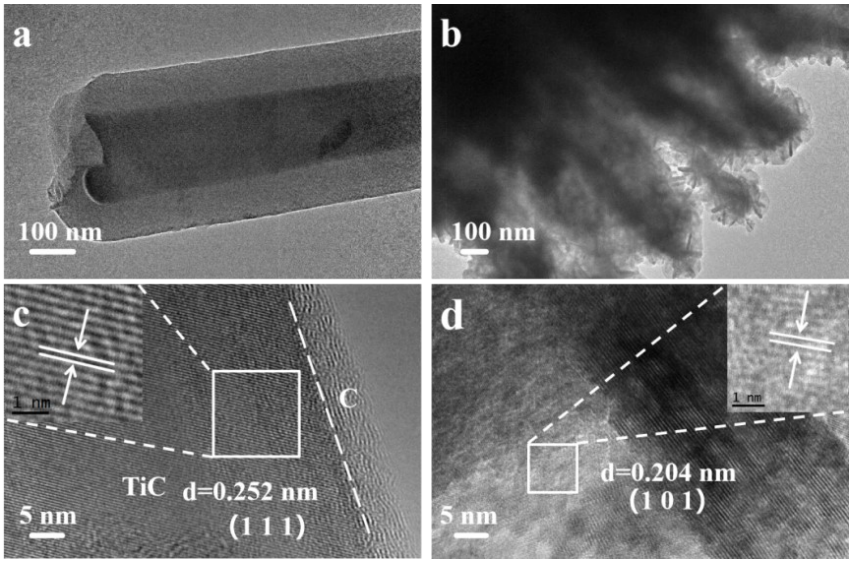

Fig. S2. TEM image of (a, c) TiC-C and (b, d) CoN/TiC-C

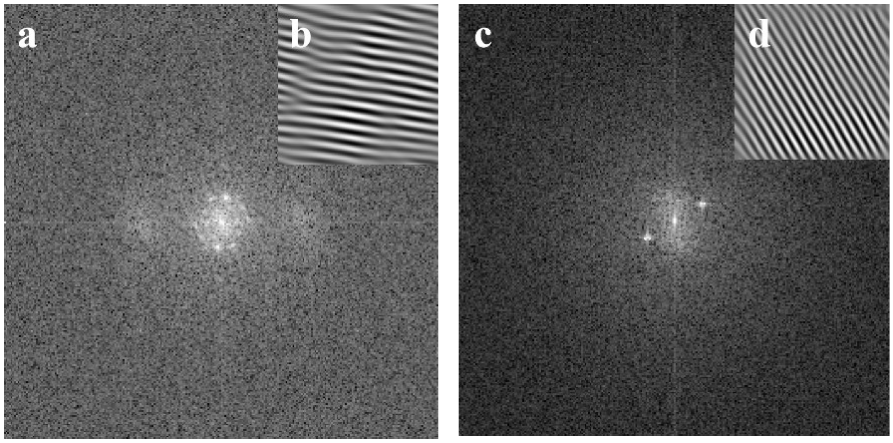

Fig. S3. HRTEM images, (a) FFT and (b) inverse FFT analyses of CoN/TiC-C. (c) FFT and (d) inverse FFT analyses of V-CoN/TiC-C

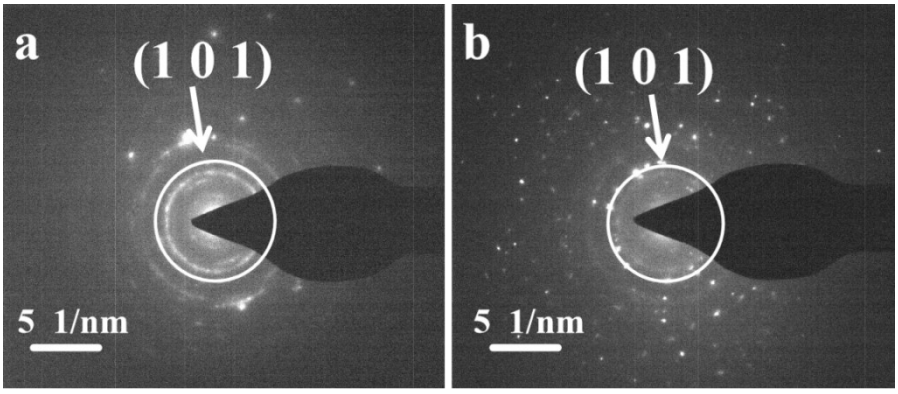

Fig. S4. Regional electron diffraction pattern of (a) TiC-C and (b) V-CoN/TiC-C

Selected-area electron diffraction (SAED) patterns (Fig. S4a) exhibit rings indexed to the TiC (101) plane, confirming its polycrystalline nature. Similarly, Fig. S4b shows distinct rings corresponding to the CoN (101) plane in V-CoN/TiC-C, providing unequivocal evidence for the successful formation of the TiC-C and V-CoN/TiC-C composite and corroborating the polycrystalline character of both components.

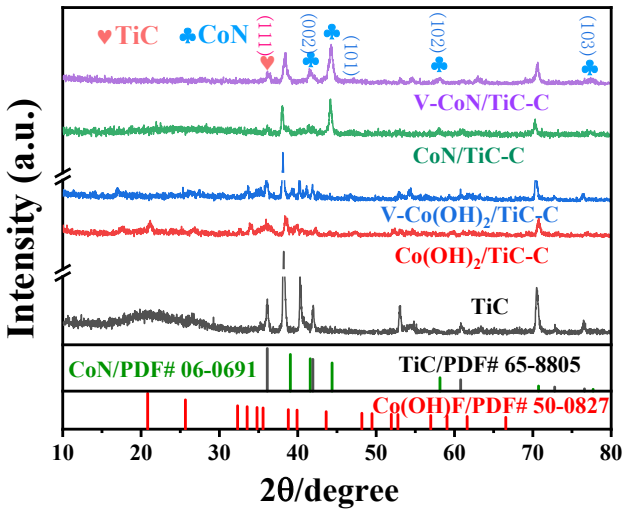

Fig. S5. XRD spectra of TiC-C, $Co(OH)_2$/TiC-C, V-$Co(OH)_2$/TiC-C, CoN/TiC-C, and V-CoN/TiC-C

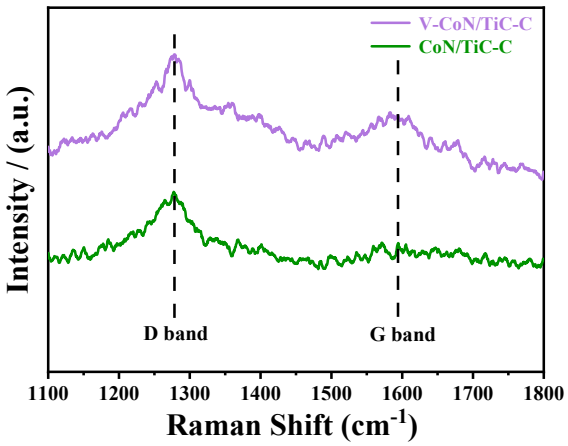

Fig. S6. Raman spectra of V-CoN/TiC-C and CoN/TiC-C

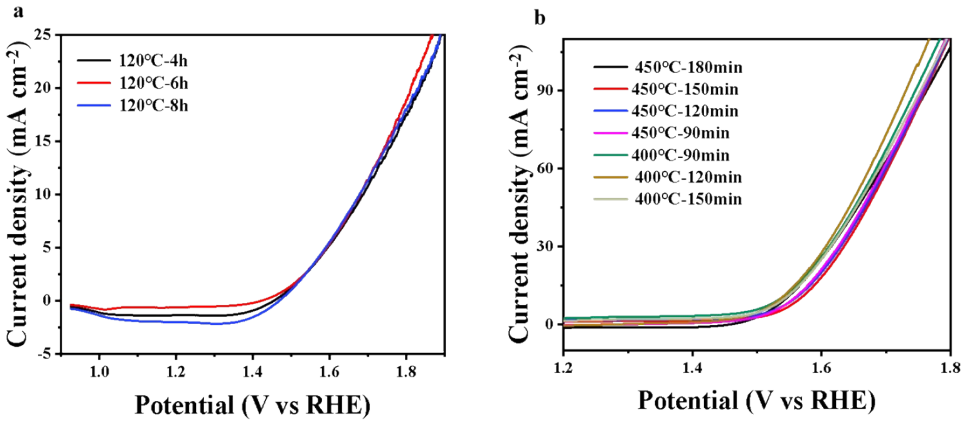

Fig. S7. (a) LSV of precursor V-Co(OH)$_2$/TiC-C with different hydrothermal times, (b) LSV of V-CoN/TiC-C with different annealing temperatures and treatment times

The hydrothermal temperature–activity relationship for V-Co(OH)$_2$/TiC-C precursors was examined by varying the dwell time at 120 °C (Fig. S7a). LSV was recorded in 1.0 M KOH using a three-electrode cell (V-Co(OH)$_2$/TiC-C on glassy carbon as working electrode, Pt foil counter, Hg/HgO reference) at 5 mV s^{-1}. Current densities increased with dwell time up to 6 h and plateaued thereafter. Consequently, 120 °C for 6 h was adopted as the optimal hydrothermal condition.

To pinpoint the optimal nitridation parameters, pre-synthesized V-Co(OH)$_2$/TiC-C precursors were subjected to NH_3 annealing under systematically varied temperatures and durations. Anneals were performed at 400 °C for 90, 120 and 150 min, and at 450 °C for 90, 120, 150 and 180 min. LSV (5 mV s^{-1}, 1.0 M KOH, three-electrode configuration) in Fig. S7b revealed that the overpotential at 10 mA cm^{-2} reached a minimum after 400 °C for 120 min. This condition was therefore adopted for all subsequent syntheses.

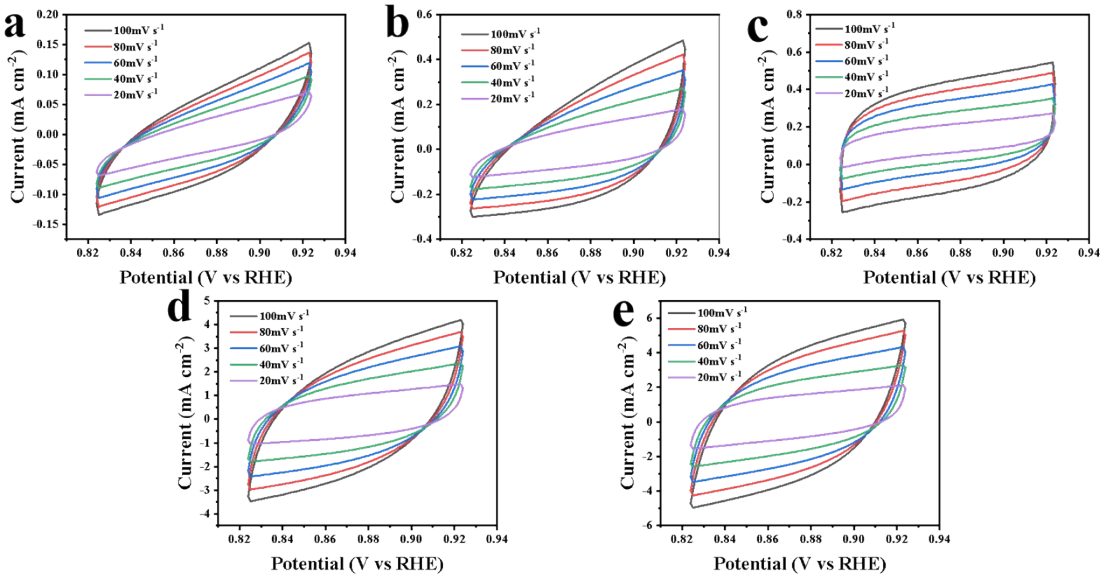

Fig. S8. CV curves of (a) TiC-C, (b) $Co(OH)_2$/TiC-C, (c) V-$Co(OH)_2$/TiC-C, (d) CoN/TiC-C and (e) V-CoN/TiC-C at different scanning rates

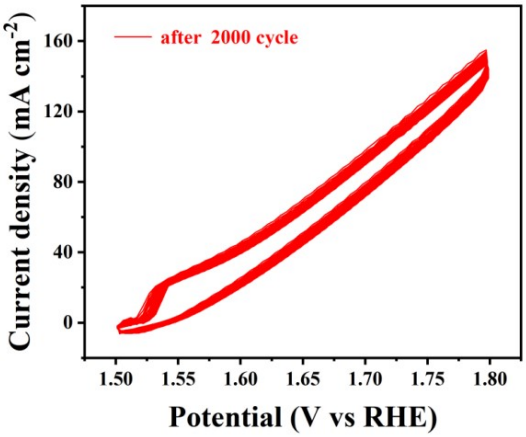

Fig. S9. CV cycle curve of V-CoN/TiC-C through 2000 cycles

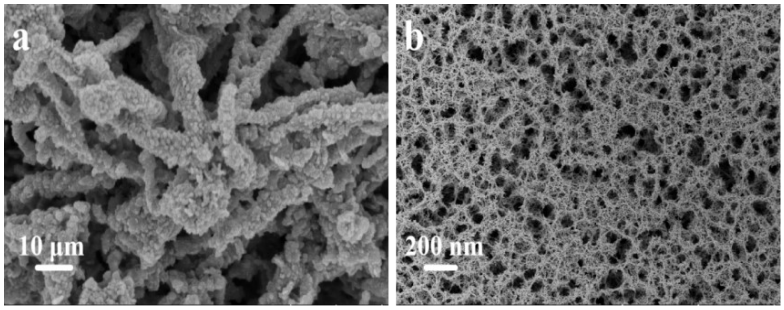

Fig. S10. (a, b) SEM images of V-CoN/TiC-C after 65 h chronopotentiometric operation at 100 mA cm^{-2}

SEM analysis (Fig. S10) reveals only minor particle agglomeration, which forms a dense, cross-linked network. The primary morphology and conductive scaffold remain intact, indicating that the crystal structure and active sites are robust enough to endure repeated redox cycles.

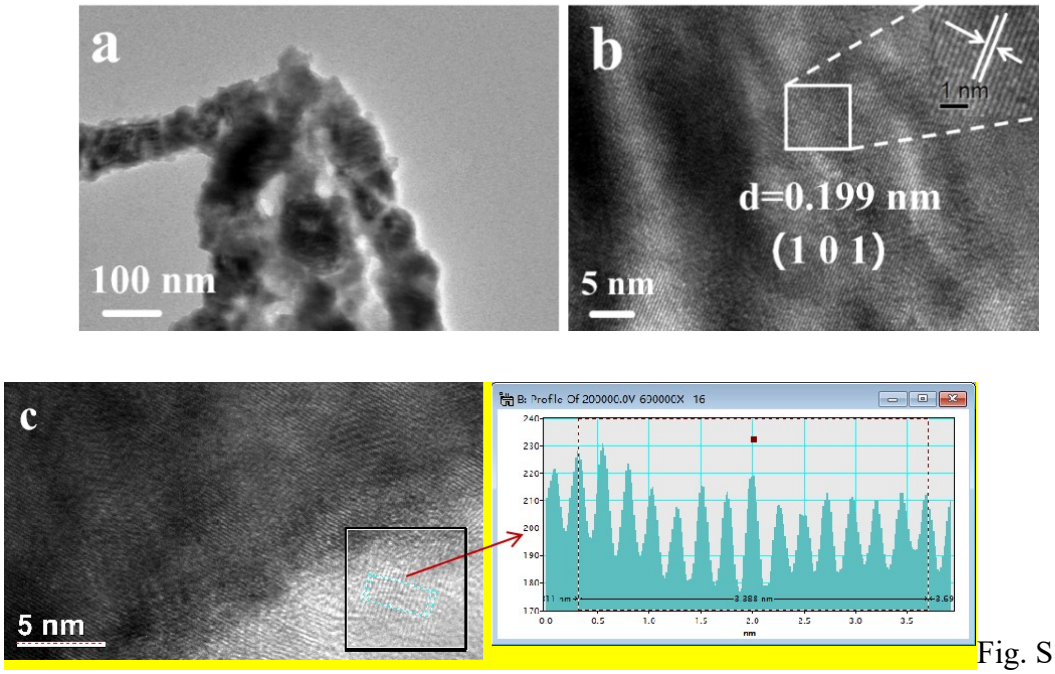

Fig. S11 (a-c) TEM images of V-CoN/TiC-C after 65 h chronopotentiometric operation at 100 mA cm^{-2}

TEM characterization (Fig. S11(a,b)) confirms that the lattice spacing remains unchanged, further demonstrating the structural stability of the catalyst. In contrast, the lattice spacing at the edge region of the spent catalyst was measured to be 0.242 nm, corresponding to the (021) plane of CoOOH (PDF #24-0480) and indicative of metal-oxygen bond formation (Fig. S11(c)). This transformation from a nitride to an oxyhydroxide phase at edge of the catalyst provides direct evidence of surface reconstruction occurring during the reaction.

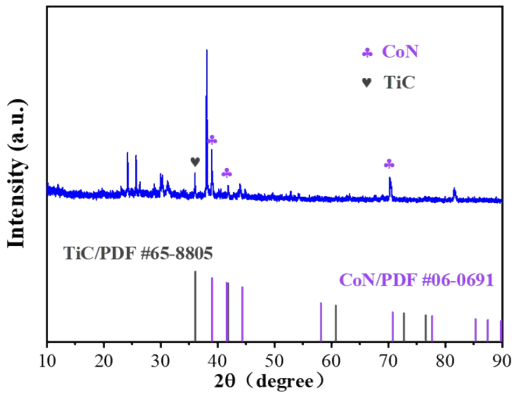

Fig. S12. XRD spectra of after 65 h chronopotentiometric operation at 100 mA cm^{-2} V-CoN/TiC-C

XRD analysis (Fig. S12) detects characteristic peaks corresponding to CoN and TiC. These results indicate that the main components of the catalyst remain stable throughout the reaction, with no significant structural changes.

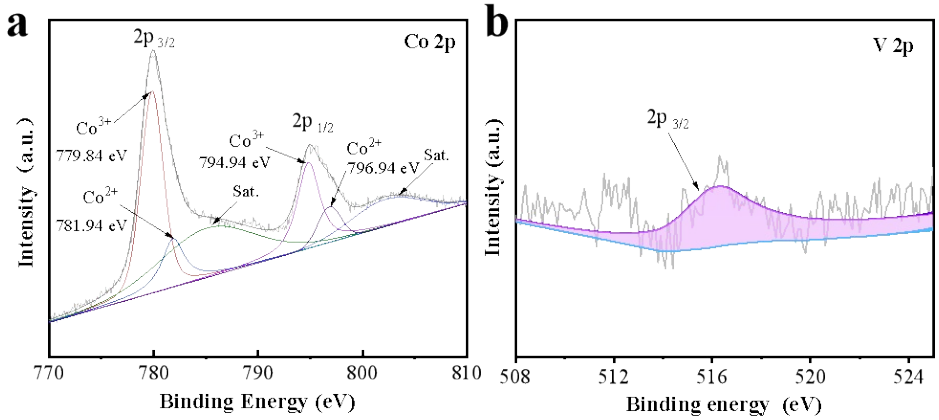

Fig. S13. High-resolution (a) Co 2p and (b) V 2p XPS spectrum of V-CoN/TiC-C after 65 h chronopotentiometric test at 100 mA cm^{-2}

Furthermore, XPS analysis of the spent catalyst (Fig. S13) provides direct evidence for surface reconstruction. The Co 2p spectrum shows negative shifts, with peaks at 779.84 eV and 794.94 eV corresponding to Co^{3+}, and peaks at 781.94 eV and 796.94 eV corresponding to Co^{2+}. This shift is characteristic of the surface transformation to $CoOOH/Co(OH)_2$ under OER conditions, consistent with the HRTEM observations. Concurrently, the V $2p_{3/2}$ peak shifts

to 516.2 eV, indicating the reduction of V^{5+} to V^{4+}. This reduction is attributed to the electron transfer associated with the surface reconstruction and the prolonged operation under high oxidative potential, which drives high-valent V towards a more stable lower oxidation state. The reduction of vanadium, coupled with the change in cobalt oxidation state, corroborates a comprehensive surface reconstruction process driven by the electrochemical environment. These chemical state evolutions confirm that the catalyst surface dynamically evolves into a $CoOOH/Co(OH)_2$-dominated phase during operation, which is key to its sustained activity.

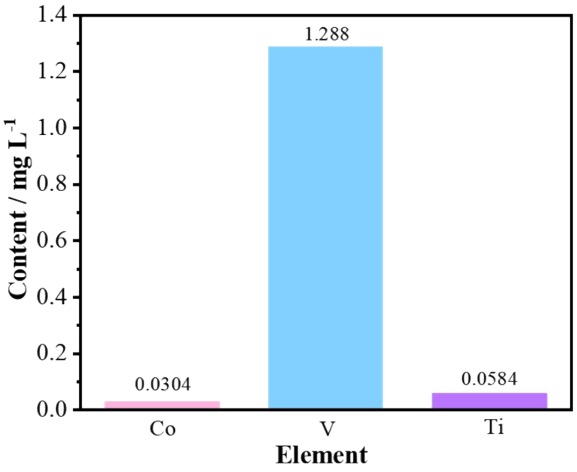

Fig. S14. Inductively coupled plasma (ICP) test of the electrolyte of V-CoN/TiC-C after 65 h chronopotentiometric test at 100 mA cm^{-2}

After the 65 h stability test, the ICP test (Fig. S14) detected a relatively high concentration of V ions in the electrolyte. This is likely due to the formation of soluble vanadates and other substances under strongly alkaline conditions, which facilitates the leaching of V from the catalyst. In contrast, the leaching levels of other metal ions (e.g., Co, Ti) remain relatively low, indicating that the catalyst possesses good chemical stability.

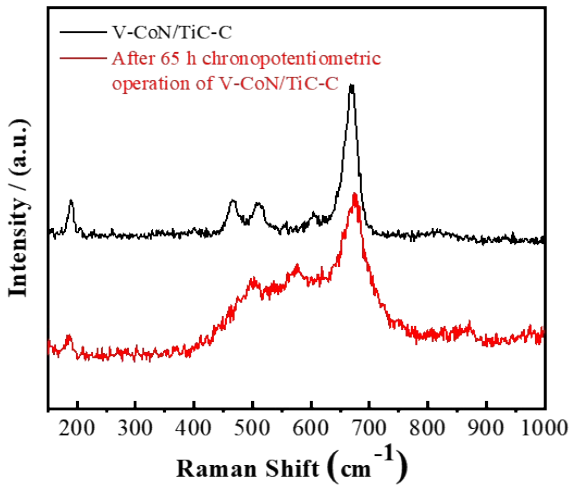

Fig. S15. Raman spectrum of V-CoN/TiC-C before and after 65 h chronopotentiometric test at 100 mA cm^{-2}

Fig. S15 presents the Raman spectrum of V-CoN/TiC-C before and after the long-term stability test, providing further insight into the surface reconstruction. Compared with the pristine catalyst, the characteristic vibrational modes in the 500–700 cm^{-1} region, initially associated with the CoN phase, undergo significant broadening and shift, indicating transformation into a cobalt oxynitride (CON) phase. This evolution directly reflects the incorporation of oxygen into the near-surface lattice during OER, creating a disordered CON structure that disrupts long-range periodicity and enhances phonon scattering. The coexistence of features attributable to both Co–O and Co–N vibrations within this broadened profile confirms the formation of a mixed oxynitride surface layer. These spectroscopic changes are fully consistent with the TEM and XPS observations, collectively reinforcing the conclusion of a dynamic surface reconstruction into an active CON/CoOOH phase under operational conditions. [1]

Table S1 Comparison of OER performance of V-CoN/TiC-C with other reported Co-based materials

Catalyst	**Electrolyte**	**Overpotential (mV)[a]**	**Ref.**

V-CoP/TiC-C	1 M KOH	238	This Work
$Co_2Fe_{0.5}V_{0.5}$ LDH	1 M KOH	242	[2]
V-$CoFe_2$/$MoTe_2$	1 M KOH	249	[3]
2D Co@S-$VMoO_x$NSs	1 M KOH	274	[4]
V-$Co_2P_4O_{12}$/CC	1 M KOH	288	[5]
V-CoS_2 NBs	1 M KOH	290	[6]
F-V-Co_3O_4	1 M KOH	320	[7]
VN-Co-P	1 M KOH	335	[8]
V-CoP	1 M KOH	340	[9]
V-$NiCo_2O_4$	1 M KOH	344	[10]

References

1 Ravikumar.MP，Quach.T-A，Manjunatha.K，Wu.SY，Do.T-O，et al., *Energy Fuels* **2025**, *39* (42), 20647–20662.

2 Yang.Y，Ou.Y，Yang.Y，Wei.X，Gao.D，et al., *Nanoscale* **2019**, *11* (48), 23296–23303.

3 Pathak.I，Muthurasu.A，Acharya.D，Chhetri.K，Dahal.B，et al., *J. Mater. Chem. A* **2024**, *12* (28), 17544–17556.

4 Wang.J，Tran.DT，Chang.K，Prabhakaran.S，Kim.DH，et al., *ACS Appl. Mater. Interfaces* **2021**, *13* (36), 42944–42956.

5 Chang.X-W，Li.S，Wang.L，Dai.L，Wu.Y-P，et al., *Advanced Functional Materials* **2024**, *34* (21), 2313974.

6 Wang.C，Xu.H，Wang.Y，Shang.H，Jin.L，et al., *Inorg. Chem.* **2020**, *59* (16), 11814–11822.

7 Xie.J-Y，Fan.R-Y，Fu.J-Y，Zhen.Y-N，Li.M-X，et al., *International Journal of Hydrogen Energy* **2021**, *46* (38), 19962–19970.

8 Yang.H，Hu.Y，Huang.D，Xiong.T，Li.M，et al., *Materials Today Chemistry* **2019**, *11*, 1–7.

9 Qin.J-F，Lin.J-H，Chen.T-S，Liu.D-P，Xie.J-Y，et al., *Journal of Energy Chemistry* **2019**, *39*, 182–187.

10 Wang.X，Zhou.Y，Luo.J，Sun.F，and Zhang.J, *Electrochimica Acta* **2022**, *406*, 139800.